

Nominal vs. actual stoichiometries in Al-doped NASICONs: A study of the $\text{Na}_{1.4}\text{Al}_{0.4}\text{M}_{1.6}(\text{PO}_4)_3$ (M=Ge, Sn, Ti, Hf, Zr) family

Pilar Maldonado-Manso^a, Miguel A.G. Aranda^a, Sebastián Bruque^a,
Jesús Sanz^b, Enrique R. Losilla^{a,*}

^aDepartamento de Química Inorgánica, Universidad de Málaga, 29071-Málaga, Spain

^bInstituto de Ciencia de Materiales, CSIC, Cantoblanco, 28049-Madrid, Spain

Received 31 January 2005; received in revised form 18 April 2005; accepted 18 April 2005

Abstract

Nominal $\text{Na}_{1.4}\text{Al}_{0.4}\text{M}_{1.6}(\text{PO}_4)_3$ (M=Ge, Sn, Ti, Hf, Zr) NASICON compounds have been prepared as polycrystalline powders. Rietveld analysis of X-ray and neutron diffraction patterns showed that M=Ge and Sn samples crystallize in the $R\bar{3}$ space group (s.g.) and that M=Ti, Hf, Zr compositions crystallize in the $R\bar{3}c$ s.g. Data analyses indicated that aluminum contents into the main NASICON phases are always smaller than the nominal ones. ²⁷Al, ³¹P and ²³Na magic angle spinning-nuclear magnetic resonance (MAS-NMR) spectroscopies have been used to deduce aluminum contents and local atomic environments. In samples with high aluminum contents, M=Ge, Sn and Ti, electrical conductivity has been deduced from impedance spectroscopy data. The titanium sample incorporates the maximum aluminum content and displays the lowest activation energy, 0.52(1) eV, and the highest conductivity, $\sigma_T(400\text{ K})=1.5(3) \times 10^{-5}\text{ S cm}^{-1}$. The influence of structural parameters on conductivity values has been analyzed with the bond valence sum method. With this technique, the most probable conduction pathways in $\text{Na}_{1+x}\text{Al}_x\text{Ti}_{2-x}(\text{PO}_4)_3$ and $\text{Na}_{1+x}\text{In}_x\text{Zr}_{2-x}(\text{PO}_4)_3$ samples have also been deduced.

© 2005 Elsevier B.V. All rights reserved.

Keywords: Fast ion conductor; Rietveld refinement; Structural correlation

1. Introduction

NASICON materials have been extensively studied because of the high conductivity shown by some compositions [1,2]. Original NASICON compounds are solid solutions derived from $\text{NaZr}_2(\text{PO}_4)_3$ by partial replacement of P by Si, where Na compensates the negatively charged framework, to give the general formula $\text{Na}_{1+x}\text{Zr}_2\text{P}_{3-x}\text{Si}_x\text{O}_{12}$ ($0 \leq x \leq 3$). The NASICON structure has a negatively charged 3D-framework, of general formula $\text{M}_2\text{X}_3\text{O}_{12}$, where the Na^+ cations reside in fully or partially-occupied sites. The framework is built of XO_4 tetrahedra linked by corners to MO_6 octahedra. Each XO_4 tetrahedron shares each corner with one MO_6 octahedron and, conversely, each

MO_6 octahedron shares each corner with a different XO_4 group. The interstitial voids generated within the network are of two types known as M1 and M2 sites (1:3 multiplicity) in the $R\bar{3}c$ space group. Na ions at the M1 sites are coordinated by a trigonal antiprism of oxygens and at the M2 site has a distorted 8-fold coordination. These sites are connected by bottlenecks generally termed M1M2 bottlenecks. Specific structural details, such as the size of the M1M2 bottleneck [3–5], are needed to understand the electrical parameters (ionic conductivities and activation energies) of these samples. Structural information can be obtained either by single-crystal diffraction or by Rietveld analysis of powder diffraction data.

In general, the properties of the NASICON-type Na^+ ion conductor compounds strongly depend upon the chemical stoichiometry, the crystal structure and unit cell parameters, that, at the same time, depend on the ionic radii of the cations located in octahedral (M) and tetrahedral (X) sites.

* Corresponding author. Tel.: +34 952134234; fax: +34 952132000.

E-mail address: r.losilla@uma.es (E.R. Losilla).

$\text{NaM}_2^{\text{IV}}(\text{PO}_4)_3$ ($\text{M}^{\text{IV}} = \text{Ti, Zr, Hf, Ge, Sn}$) samples have been widely studied [6–8]. They are versatile materials that can tolerate a wide range of compositions. Many attempts have been reported on the partial substitution with pentavalent [9], tetravalent [10–13] and trivalent [14,15] cations on the octahedral site. In each case, the compositional limit depends on the nature and ionic radii of the octahedral cations. In this view, we have previously reported a study of the $\text{Na}_{1.4}\text{In}_{0.4}\text{M}_{1.6}(\text{PO}_4)_3$ ($\text{M} = \text{Ti, Sn, Hf, Zr}$) NASICON compounds [16]. The characterization of this family of compounds was carried out by using several techniques: X-ray diffraction, ^{23}Na and ^{31}P MAS-NMR and impedance spectroscopies. A similar multitechnique study, enhanced by employing neutron diffraction data, was undertaken in $\text{Na}_{1+x}\text{In}_x\text{Zr}_{2-x}(\text{PO}_4)_3$ ($0 \leq x \leq 2$) NASICON series [17].

On the other hand, there are few reports of NASICON materials containing Al cations. These works mainly deal with lithium based ionic conductors. In the ceramic synthesis of these materials, AlPO_4 type side-compounds can be formed. Phases as berlinite, containing tetrahedral AlO_4 groups, are very stable and once formed do not yield the desired material. We have recently reported [18] that the $\text{Na}_{1+x}\text{Al}_x\text{Ti}_{2-x}(\text{PO}_4)_3$ ($0 \leq x \leq 0.9$) NASICON series can be stabilized using an adequate synthetic method with very low aluminum side-phase contents.

In the present work, we have analyzed the dependence of mobility of the charge carriers with the structure and geometry of the conduction pathways in nominal $\text{Na}_{1.4}\text{Al}_{0.4}\text{M}_{1.6}(\text{PO}_4)_3$ ($\text{M} = \text{Ge, Sn, Ti, Hf, Zr}$) NASICON compounds. These five samples have been chosen to analyze the influence of the smaller Al^{3+} cations on the electrical conductivity of NASICON compounds. For that, composition, structure and electrical conductivity have been determined by using: laboratory X-ray and neutron powder diffraction, ^{27}Al , ^{31}P and ^{23}Na MAS-NMR spectroscopies and impedance spectroscopy.

2. Experimental

The NASICON phases were prepared from stoichiometric amounts of MO_2 ($\text{M} = \text{Ge, Sn, Ti, Hf, Zr}$), Na_2CO_3 , $\gamma\text{-Al}_2\text{O}_3$ and $(\text{NH}_4)_2\text{HPO}_4$. MO_2 ($\text{M} = \text{Ti, Zr}$) were synthesized by slow hydrolysis with 1:4 water-to-propanol solution of commercial alkoxides: 97% $\text{Ti}(\text{OCH}(\text{CH}_3)_2)_4$ and solution of 70% $\text{Zr}[\text{OCH}_2\text{CH}_2\text{CH}_3]_4$ in 1-propanol. The resulting white suspensions were centrifuged, washed thoroughly with water and heated at 573 K for 24 h. SnO_2 was prepared from commercial SnCl_4 by hydrolysis with $\text{NH}_3(\text{aq})$ to pH 8. The white solid was centrifuged, washed with water to pH 7, and heated at 473 K for 24 h. MO_2 ($\text{M} = \text{Ti, Sn, Zr}$) solids showed amorphous X-ray powder diffraction profiles. A part of each sample was heated at 1273 K for 12 h to determine the small weight loss due to the residual water, this was taken into account when preparing the stoichiometric reagent mixtures. HfO_2 (Aldrich, 98.0%) with

microparticle size $< 1 \mu\text{m}$ and GeO_2 (Aldrich, 99.998%) was dried at 473 K and used without further treatments.

The synthesis of $\text{Na}_{1.4}\text{Al}_{0.4}\text{M}_{1.6}(\text{PO}_4)_3$ ($\text{M} = \text{Ge, Sn, Ti, Hf, Zr}$) samples has been optimized by the choice of heating temperatures, rates and times. The synthetic procedure used was: (1) the reagents were ground in an agate mortar for 20 min and heated in platinum crucibles at 0.1 K min^{-1} up to 473 K for 4 h; (2) then, the mixtures were heated up to 573 K for 8 h in order to ensure total decomposition of reagents; (3) after cooling, the samples were ground and homogenized for 30 min in agate bowls of a Pulverisette Fritsch mill working at 200 rpm with reversed rotation each 10 min; (4) the mixtures were pelletized and a second thermal treatment was carried out at 998 K ($\text{M} = \text{Ge, Ti}$) and 1373 K ($\text{M} = \text{Sn, Hf, Zr}$) for 24 h; after that, (5) $\text{M} = \text{Ge, Ti}$ samples were ground for another 15 min in the agate mortar, pelletized and heated again at 1073 K for 3 h; (6) finally, after 20 min homogenization in the mill, the samples were heated at 1123 K for 70 h ($\text{M} = \text{Ge, Ti}$) and 1373 K for 14 h ($\text{M} = \text{Sn, Hf, Zr}$). For the sake of comparison, stoichiometric $\text{NaM}_2(\text{PO}_4)_3$ ($\text{M} = \text{Ge, Sn, Ti, Hf, Zr}$) samples were prepared, as described above for aluminum-doped samples.

2.1. Powder diffraction

All the samples were characterized by laboratory X-ray powder diffraction (LXRPD) at room temperature. The powder patterns were collected on a Siemens D5000 automated diffractometer with $(\theta/2\theta)$ Bragg–Brentano geometry using graphite monochromated $\text{CuK}_{\alpha 1,2}$ radiation between 19° and 120° (2θ) with 0.03° step size counting for 15 s.

Room temperature neutron powder diffraction (NPD) patterns were collected on the HRPT diffractometer [19] [SINQ neutron source at Paul Scherrer Institute, Villigen, Switzerland] for $\text{M} = \text{Ge, Sn, Ti}$ and Hf materials. The samples were loaded in a vanadium can. HRPT was used in the “medium-resolution” mode with a wavelength of $\sim 1.886 \text{ \AA}$ which was selected by the (511) reflection of the vertically-focusing Ge monochromator. To have good statistics, the measuring time was $\approx 8 \text{ h}$ per pattern. The 2θ angular range analyzed was $5\text{--}165^\circ$ [$21\text{--}0.95 \text{ \AA}$] with 0.1° step size. Structural data were deduced from the joint LXRPD and NPD Rietveld [20] refinement by using the GSAS suite of programs [21]. In order to measure the overall amorphous content of the material [22], the germanium-containing NASICON sample was mixed with MgO (20.01 wt.%), prior to the NPD data collection.

Differential thermal analysis data were recorded for all compositions on a Setaram Labsys apparatus. The temperature was varied from room temperature up to 1473 K at a heating rate of 10 K min^{-1} with calcinated Al_2O_3 taken as reference.

^{27}Al , ^{31}P and ^{23}Na MAS-NMR spectra were recorded at room temperature in an MSL 400 Bruker spectrometer working at 104.2, 161.9 and 105.8 MHz, respectively.

Samples were spun at 10–12 kHz and spectra taken after $\pi/2$ pulse irradiations (2–6 μ s). The number of scans was in the range of 40–200, and the time between scans was selected between 5 and 60 s, according to the spin-lattice relaxation of the analyzed nuclei. Chemical shifts of NMR signals are given relative to the aqueous solutions AlCl_3 (1M), H_3PO_4 (85 wt.%) and NaCl (1M). The analysis of NMR spectra was carried out with the Winfit (Bruker) software package [23]. Deconvolution used a standard, nonlinear least-squares fitting method. The spinning rate, position, line width, and intensity of components are automatically determined. However, chemical shift anisotropies and quadrupole constants are adjustable parameters that must be determined by trial and error procedures. In particular, an estimation of second-order quadrupole interactions, responsible for the detection of three peaks for Na atoms in M1 site, is necessary before analysis of M2 site occupancy.

Impedance data for M=Ge, Sn, Ti samples were collected on cylindrical pellets (~ 10 mm of diameter and ~ 2 mm of depth) obtained by applying an uniaxial pressure of 150 MPa for 1 min in a 10-mm die. The pellets were heated at 1273 K for 3 h (M=Ge), 998 K for 24 h (M=Ti) and 1423 K for 2 h (M=Sn) and quenched to room temperature. The porosities estimated from the pellets mass and geometry were approximately below 10%. Electrodes were made by sputtering gold on opposite pellet faces. The impedance data were collected by using a Hewlett-Packard 4284 impedance analyzer over the frequency range from 20 Hz to 1 MHz with an applied voltage of 0.1 V. Samples were studied at 238 and 248 K and in two more temperature ranges: (i) from 273 to 423 K (at 25 K intervals) and (ii) from 523 to 623 K (at 50 K intervals) in a Novocontrol Quatro Cryosystem. All measurements were done under a dried nitrogen atmosphere. Stabilization time before data acquisition was 40 min. Measurement processes were controlled electronically by the winDeta package of programs [24].

3. Results

3.1. Rietveld study

LXRPD data indicated that the main crystalline phase in the five members of this series have NASICON-type structure. M=Ti, Hf, Zr samples crystallize in the $R\bar{3}c$ s.g. and M=Ge, Sn compounds crystallize in the $R\bar{3}$ s.g. For these two samples, some diffraction peaks [i.e. at 33.9 and 40.4° (2θ) for M=Ge and 32.3 and 38.5° (2θ) for M=Sn] can only be indexed in the maximal non-isomorphic subgroup $R\bar{3}$. A minor crystalline side-phase, AlPO_4 with powder diffraction file (PDF) number 48-0652, was detected in all samples; as well as traces of GeO_2 (PDF 83-2474) for M=Ge, SnO_2 (PDF 41-1445) for M=Sn and NaAlP_2O_7 (PDF 84-2483) for M=Ti. Thermal analysis

showed the absence of phase transitions and weight losses between room temperature and 1473 K.

NPD patterns have been collected for M=Ge, Sn, Ti and Hf compositions in order to accurately locate the oxygen positions and to verify the Al/M compositions deduced from the NMR data (see below). Thus, joint LXRPD and NPD Rietveld refinements [20] were carried out. The crystal structures of the four nominal NASICON phases, $\text{Na}_{1.4}\text{Al}_{0.4}\text{M}_{1.6}(\text{PO}_4)_3$ (M=Ge, Sn, Ti, Hf), were refined using the structures of parent compounds $\text{NaSn}_2(\text{PO}_4)_3$ $R\bar{3}$ s.g. [7], inorganic crystal structure database (ICSD) number 72215; $\text{NaM}_2(\text{PO}_4)_3$ (M=Ti, ICSD 80426, [25]; Zr ICSD 9546, [26]) $R\bar{3}c$ s.g. as starting models.

Initially, the nominal Al/M composition was assumed to be randomly distributed at the octahedral site. A full occupancy of the Na(1) site and a partial occupation of Na(2) sites was initially postulated. The common overall parameters, histogram scale factor, background coefficients, unit cell parameters, zero-shift error and pseudo-Voigt coefficients [27] corrected for asymmetry [28] were refined. Then, the positional parameters were optimized. After convergence, the Al/M occupation factors were allowed to vary but constrained to full occupancy. The crystal structures of the M=Ti, and Hf samples ($R\bar{3}c$) have a unique octahedral site but those of the M=Ge, and Sn samples ($R\bar{3}$) have two different octahedral sites, *a* and *b*. There is no evidence of vacancies at the Na(1) site for the four compounds so their occupation factors were fixed to 1.0. The refined occupation factors of Na(2) were freely refined and they converged to values in good agreement with the molar aluminum contents. Finally, isotropic temperature factors were freely refined but those of the Na(2) site were fixed to reasonable values, $U_{\text{iso}}=0.03 \text{ \AA}^2$, due to their low occupancies. Weight fractions of secondary phases were also refined. Temperature factors for the sodium cations were not refined anisotropically due to the insufficient quality of the powder diffraction data.

The four samples have AlPO_4 (PDF 48-0652) as side-phase and the refined contents are given in Table 1. M=Ge sample also contains GeO_2 0.74(3) wt.%; M=Ti sample also contains NaAlP_2O_7 2.5(1) wt.%; M=Sn also contains SnO_2 0.37(2) wt.%. Final refined unit cell parameters deduced from LXRPD data refinements for $\text{Na}_{1.4}\text{Al}_{0.4}\text{M}_{1.6}(\text{PO}_4)_3$ and $\text{NaM}_2(\text{PO}_4)_3$ (M=Ge, Sn, Ti, Hf, Zr) samples are given in Table 1.

Final Rietveld disagreement factors were good (Table 1), with R_F values for NPD lower than 5% for all NASICON phases. Atomic parameters of the $R\bar{3}$ (M=Ge, Sn) and $R\bar{3}c$ (M=Ti, Hf) phases are given in Tables 2 and 3, respectively. Selected inter-atomic distances and bond angles of M=Ge, Ti, Sn and Hf are given as Supplementary material, Tables I to IV, respectively. As an example of the Rietveld refinements quality, the fits of the LXRPD and NPD data for nominal $\text{Na}_{1.4}\text{Al}_{0.4}\text{Ti}_{1.6}(\text{PO}_4)_3$ are shown in Figs. 1 and 2, respectively.

Table 1

Some crystallographic parameters, Rietveld disagreement factors, M–O average bond distances for nominal $\text{Na}_{1.4}\text{Al}_{0.4}\text{M}_{1.6}(\text{PO}_4)_3$ (M=Ge, Sn, Ti, Hf and Zr) samples and weight fraction of AlPO_4 from the Rietveld refinements

M	x	a/Å	c/Å	V/Å ³	<i>R</i> _{wp} [*] /%	<i>R</i> _p [*] /%	<i>R</i> _F [*] /%	<M–O>/Å	AlPO ₄ /%
Ge	0	8.0966(1)	21.5437(2)	1223.09(2)				1.871(7)	
	0.4	8.1427(1)	21.5000(4)	1234.54(5)	8.64 <i>3.79</i>	6.74 <i>2.96</i>	1.91 <i>2.23</i>	1.861(5)	5.2(1)
Sn	0	8.5120(1)	22.5000(4)	1411.80(4)				2.034(9)	
	0.4	8.5346(1)	22.3847(4)	1412.03(5)	8.87 <i>1.21</i>	6.66 <i>0.90</i>	1.94 <i>4.63</i>	2.015(7)	1.9(3)
Ti	0	8.4627(4)	21.935(1)	1360.5(2)				1.937(5)	
	0.4	8.4748(2)	21.7690(7)	1354.03(9)	12.68 <i>4.82</i>	9.72 <i>3.76</i>	2.49 <i>2.84</i>	1.924(2)	2.9(2)
Hf	0	8.7777(1)	22.6857(4)	1513.72(4)				2.103(7)	
	0.4	8.7659(1)	22.7027(5)	1510.80(6)	8.19 <i>4.99</i>	6.24 <i>3.91</i>	1.80 <i>4.96</i>	2.053(2)	3.2(2)
Zr	0	8.8088(1)	22.7689(3)	1530.04(4)				2.082(4)	
	0.4	8.7973(3)	22.732(1)	1523.6(1)	13.32	8.83	6.69	1.975(5)	9.6(7)

Cell parameters and M–O average bond distances for $\text{NaM}_2^{IV}(\text{PO}_4)_3$ (M=Ge, Sn, Ti, Hf and Zr) are also given for comparison.

*NPD R-factors are given in italics. *R*_{wp}, *R*_p and *R*_F stand for weight-profile, profile and structure factor Rietveld disagreement factors.

Nominal $\text{Na}_{1.4}\text{Al}_{0.4}\text{Ge}_{1.6}(\text{PO}_4)_3$ sample was mixed with 20.01 wt.% of MgO before the NPD experiment. The results given above in Tables 1 and 2 and Table I (Supplementary material) were obtained by the joint refinement of LXRPD and NPD data by excluding the five peaks of MgO. With the final structural description for the NASICON phase plus the impurities (AlPO_4 and GeO_2), we carried out a full phase analysis, and the Rietveld refined phase fraction for MgO was 22.7(1) wt.%. There is an overestimation, 2.7 wt.%, because of the presence of an amorphous phase in the NASICON material. This overestimation gives the overall non-diffracting content, 14.8 wt.%, according to the reported conversion formula [22].

3.2. ²⁷Al MAS-NMR study

The room temperature ²⁷Al MAS-NMR spectra of the five samples, Fig. 3, are formed by at least two components with their corresponding spinning sidebands (not shown). The bands located close to –15 ppm correspond to AlO_6 environments and the other broader absorptions, with maximum at ~39 ppm, are due to AlO_4 environments. The AlO_6 band is mainly due to Al in the octahedral site of the NASICON structure and it undergoes a higher shielding effect (the chemical shifts move to more negative values) as tetravalent cation radii increases, see Fig. 3. In accordance with structural information, there is only one NMR signal in the M=Ti, Hf and Zr phases (*R*_{3c} s.g.). In the last two

Table 2

Refined structural parameters obtained from combined LXRPD and NPD refinements for $\text{Na}_{1.13}\text{Al}_{0.13}\text{Ge}_{1.87}(\text{PO}_4)_3$ and $\text{Na}_{1.15}\text{Al}_{0.15}\text{Sn}_{1.85}(\text{PO}_4)_3$ in *R*_{3̄} s. g.

M	Atom	x	y	z	Occupation factor	<i>U</i> _{iso} × 100/Å ²
Ge	Na(1a) (3a)	0	0	0	1.00	5.8(5)
	Na(1b) (3b)	0	0	0.5	1.00	0.5(3)
	Na(2) (18f)	0.65 ^a	0 ^a	0.25 ^a	0.042(3)	3.0 ^a
	(Al–Ge)(1a) (6c)	0	0	0.1473(2)	0.127(9)/0.873(9)	0.38(9)
	(Al–Ge)(1b) (6c)	0	0	0.6445(2)	0.0/1.0	1.7(1)
	P (18f)	0.2872(4)	0.0021(6)	0.2489(2)	1.00	0.27(5)
	O(1a) (18f)	0.1481(5)	–0.0689(5)	0.1946(1)	1.00	0.6(1)
	O(1b) (18f)	0.0150(5)	–0.1801(6)	0.6901(2)	1.00	1.2(1)
	O(2a) (18f)	0.2042(5)	0.1371(5)	0.0936(2)	1.00	0.79(9)
	O(2b) (18f)	–0.1839(5)	–0.1752(5)	0.5886(2)	1.00	0.9(1)
Sn	Na(1a) (3a)	0	0	0	1.00	6.7(9)
	Na(1b) (3b)	0	0	0.5	1.00	1.9(5)
	Na(2) (18f)	0.65 ^a	0 ^a	0.25 ^a	0.056(6)	3.0 ^a
	(Al–Sn)(1a) (6c)	0	0	0.1479(1)	0.0/1.0	0.4(1)
	(Al–Sn)(1b) (6c)	0	0	0.6451(2)	0.148(9)/0.852(9)	0.2(1)
	P (18f)	0.2910(5)	0.0024(9)	0.2516(4)	1.00	0.87(8)
	O(1a) (18f)	0.194(1)	–0.0128(7)	0.1934(3)	1.00	2.5(2)
	O(1b) (18f)	0.0466(8)	0.830(1)	0.6957(3)	1.00	2.1(2)
	O(2a) (18f)	0.1756(6)	0.1826(6)	0.0869(2)	1.00	0.2(1)
	O(2b) (18f)	0.8504(6)	0.7946(7)	0.5903(2)	1.00	1.0(1)

^a Fixed value due to the low occupation factor.

Table 3

Refined structural parameters obtained from combined LXRPD and NPD refinement for $\text{Na}_{1.30}\text{Al}_{0.30}\text{Ti}_{1.70}(\text{PO}_4)_3$ and $\text{Na}_{1.09}\text{Al}_{0.09}\text{Hf}_{1.91}(\text{PO}_4)_3$ in $R\bar{3}c$ s.g.

M	Atom	x	y	z	Occupation factor	$U_{\text{iso}} \times 100/\text{\AA}^2$
Ti	Na(1) (6b)	0	0	0	1.00	4.1(2)
	Na(2) (18e)	0.658(4)	0	0.25	0.087(6)	3.0 ^a
	Al/Ti (12c)	0	0	0.1457(1)	0.152(6)/0.848(6)	0.21(7)
	P (18e)	0.2869(2)	0	0.25	1.00	0.76(5)
	O(1) (36f)	0.1729(3)	−0.0256(2)	0.1929(1)	1.00	1.48(5)
	O(2) (36f)	0.1920(2)	0.1650(3)	0.0893(1)	1.00	1.08(5)
Hf	Na(1) (6b)	0	0	0	1.00	3.8(2)
	Na(2) (18e)	0.69(1)	0	0.25	0.031(7)	3.0 ^a
	Al/Hf (12c)	0	0	0.14563(4)	0.046(6)/0.954(6)	0.44(3)
	P (18e)	0.2912(2)	0	0.25	1.00	0.86(6)
	O(1) (36f)	0.1829(2)	−0.0187(2)	0.19532(6)	1.00	1.51(4)
	O(2) (36f)	0.1936(2)	0.1690(2)	0.08759(6)	1.00	1.35(4)

^a Fixed value due to the low occupation factor.

samples, the spectra show also a small shoulder (marked with asterisks) associated with AlO_6 environments of amorphous non identified phases. For $R\bar{3}$ compositions ($M=\text{Ge}, \text{Sn}$), there are two non-equivalent octahedral sites that produce two NMR signals. Accordingly, at least two bands can be seen in the $M=\text{Sn}$ spectrum (AlO_6 region), but they are not so clearly resolved in the analogous region of the $M=\text{Ge}$ spectrum, see Fig. 3.

The AlO_4 band is mainly due to the AlPO_4 phase, detected and quantified by X-ray diffraction (see Table 1). The ^{27}Al MAS-NMR spectra have been quantitatively analyzed, and the overall octahedral and tetrahedral alumi-

num ratios are given in Table 4. From the overall AlO_6 content, and subtracting the contribution of the side-phases, it is possible to calculate the aluminum content in the NASICON phase. These values are also given in Table 4 and they are lower than the nominal stoichiometry ($x=0.4$).

3.3. ^{31}P MAS-NMR study

Room temperature ^{31}P MAS-NMR spectra of the samples, Fig. 4, are formed by a group of bands, one of them considerably more intense than the others. The corresponding spinning sidebands of these components

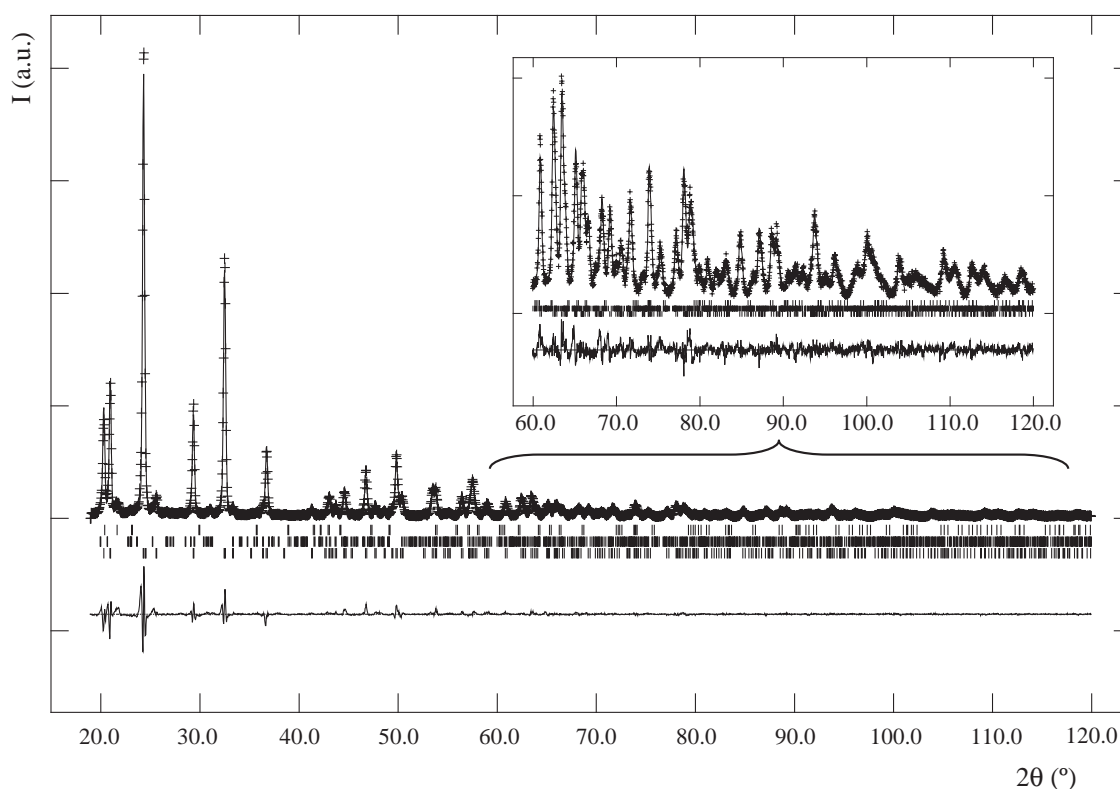


Fig. 1. Observed, calculated and difference laboratory X-ray diffraction patterns for nominal $\text{Na}_{1.4}\text{Al}_{0.4}\text{Ti}_{1.6}(\text{PO}_4)_3$. Reflections positions correspond, from top to bottom, to AlPO_4 , NaAlP_2O_7 and NASICON phase.

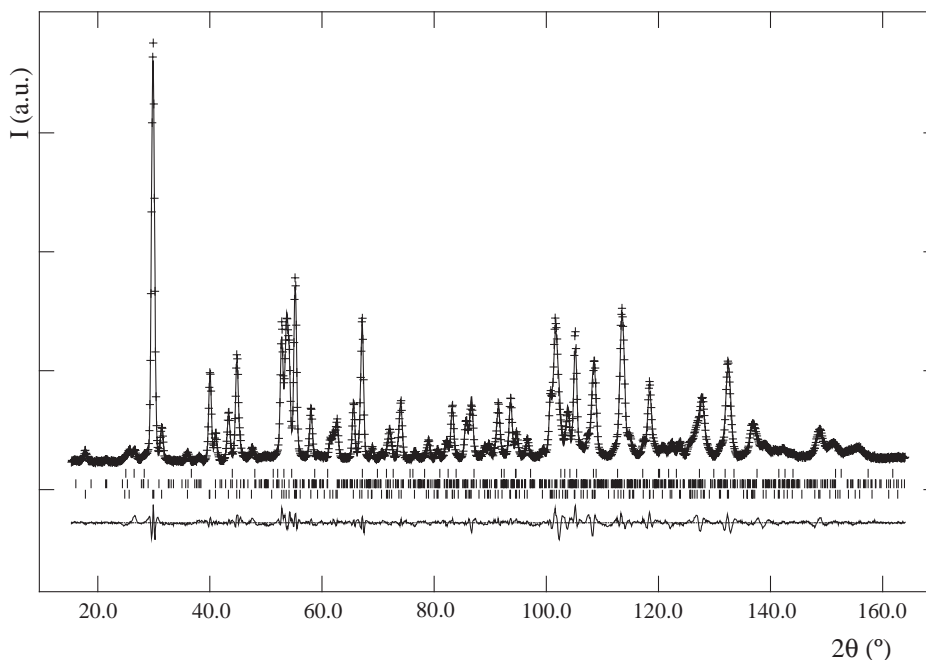


Fig. 2. Observed, calculated and difference neutron diffraction patterns for nominal $\text{Na}_{1.4}\text{Al}_{0.4}\text{Ti}_{1.6}(\text{PO}_4)_3$. The reflections positions order as in Fig. 1.

have not been analyzed (not shown). The $\text{M}=\text{Ti}$ spectrum exhibits a small band at ~ -19.7 ppm that corresponds to NaAlP_2O_7 , detected and quantified by X-ray diffraction.

In the NASICON structure, each tetrahedron shares oxygens with four octahedra. On the basis of a random distribution of tri- and tetravalent cations, five possible environments for P atoms can be envisaged in the $\text{Na}_{1.4}\text{Al}_{0.4}\text{M}_{1.6}(\text{PO}_4)_3$ phases: $\text{P}(\text{OM})_4$, $\text{P}(\text{OM})_3(\text{OAl})$, $\text{P}(\text{OM})_2(\text{OAl})_2$, $\text{P}(\text{OM})(\text{OAl})_3$ and $\text{P}(\text{OAl})_4$. From statistical considerations [17], the highest detected component must correspond to the first environment, $\text{P}(\text{OM})_4$. The variation observed in the position of the $\text{P}(\text{OM})_4$ “main” signal in the five samples is associated with differences in

the polarizing strength of the tetravalent cation, see Table 5. In general, cations with smaller radii pull the electron density away from oxygen atoms more effectively, leaving the phosphorus atoms more positively charged. This produces a higher shielding effect on the ^{31}P NMR resonance, which explains the more negative σ_{iso} values observed for ($\text{M}=\text{Zr}$, Sn , Ti , Ge). For the $\text{M}=\text{Hf}$ sample, the $\text{P}(\text{OHf})_4$ signal is located to a more positive chemical shift value, -16.9 ppm, than that of the Zr phase, likely due to the role of the f-electrons in the shielding of the phosphorous atom. In order to analyze the chemical shift positions for $\text{P}(\text{OM})_3(\text{OAl})$, $\text{P}(\text{OM})_2(\text{OAl})_2$, $\text{P}(\text{OM})(\text{OAl})_3$ bands, we speculate that the position of the component

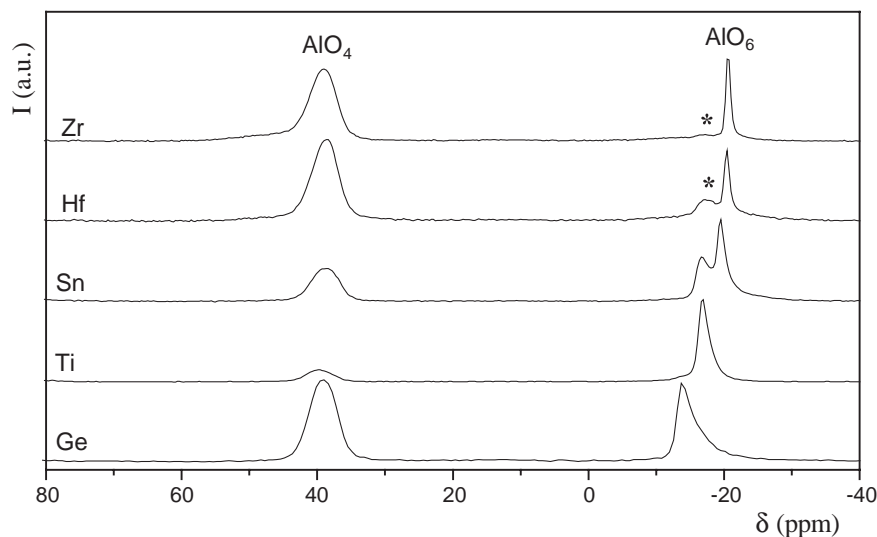


Fig. 3. Centerbands of ^{27}Al MAS-NMR spectra for nominal $\text{Na}_{1.4}\text{Al}_{0.4}\text{M}_{1.6}(\text{PO}_4)_3$ ($\text{M}=\text{Ge}$, Sn , Ti , Hf and Zr) samples. AlO_4 and AlO_6 represent tetrahedral and octahedral aluminum, respectively.

Table 4

Quantitative analysis results of ^{27}Al MAS-NMR spectra for nominal $\text{Na}_{1.4}\text{Al}_{0.4}\text{M}_{1.6}^{\text{IV}}(\text{PO}_4)_3$ (M=Ge, Sn, Ti, Hf and Zr) samples

	$\text{AlO}_4^{\%}/\%$	$\text{AlO}_6^{\%}/\%$	Al_x
Ge	55.94	44.06	0.12
Sn	33.93	66.07	0.19
Ti	21.68	78.32	0.31
Hf	64.68	35.32	0.04
Zr	73.90	26.10	0.06

Aluminum molar contents in the NASICON phase (Al_x), subtracting the contribution of side-phases, are also given.

^aOverall Al in tetrahedral environments: AlPO_4 and the amorphous phases.

^{*}Overall Al in octahedral environments: NASICON phases, NaAlP_2O_7 and the amorphous phases.

associated with the hypothetical “ $\text{Na}_3\text{Al}_2(\text{PO}_4)_3$ ” NASICON compound, should be close to -20 ppm. Thus, on the basis of the regular separation between components, the mixed environments, $\text{P}(\text{OM})_{4-x}(\text{OAl})_x$, can be estimated, see Table 5.

Due to the low aluminum content introduced, see Table 4, only the first three environments have been considered (Table 5). For $R\bar{3}c$ compositions (M=Ti, Hf, Zr), the $\text{P}(\text{OM})_4$, $\text{P}(\text{OM})_3(\text{OAl})$ and $\text{P}(\text{OM})_2(\text{OAl})_2$ components yield three bands; for $R\bar{3}$ compositions (M=Ge, Sn), the existence of two non-equivalent octahedral sites multiplies the number of environments, which increases to six: $\text{P}(\text{OM})_4$, $\text{P}(\text{OM})_3(\text{OAl})^a$, $\text{P}(\text{OM})_3(\text{OAl})^b$, $\text{P}(\text{OM})_2(\text{OAl})_2^a$, $\text{P}(\text{OM})_2(\text{OAl})_2^b$ and $\text{P}(\text{OM})_2(\text{OAl})^a(\text{OAl})^b$. From the integrated intensities of the observed ^{31}P MAS-NMR bands, the chemical composition of samples has been determined. In particular, Al/M ratios can be calculated from the expression:

$$\text{Al}/\text{M} = \frac{4I_0 + 3I_1 + 2I_2 + I_3}{I_1 + 2I_2 + 3I_3 + 4I_4} \quad (1)$$

where intensities I_i , with $i=0, 1, 2, 3$ and 4, correspond to components with an increasing number of Al atoms. From

Table 5

Chemical shift of ^{31}P MAS-NMR components for $\text{Na}_{1.4}\text{Al}_{0.4}\text{M}_{1.6}^{\text{IV}}(\text{PO}_4)_3$ (M=Ge, Sn, Ti, Hf and Zr) samples

	$\text{P}(\text{OM})_4$	$\text{P}(\text{OM})_3(\text{OAl})$	$\text{P}(\text{OM})_2(\text{OAl})_2$	Al_x
Ge	-38.18	$-35.44/-34.02$	$-29.60/-28.34/-27.01$	0.08
Sn	-25.40	$-24.23/-23.84$	$-22.65/-21.34/-20.34$	0.15
Ti	-27.61	-26.52	-24.85	0.21
Hf	-16.89	-18.44	-19.56	0.05
Zr	-24.04	-22.79	-21.95	0.05

Aluminum molar contents (Al_x), indirectly obtained from the quantitative analysis, are also included.

Al/M ratios, the M ($2-x$) and Al (x) contents of octahedra can be deduced, using the expression:

$$\text{Al}/\text{M} = (2-x)/x. \quad (2)$$

The obtained aluminum occupancies, Table 5, are lower than the nominal values and close to the contents obtained from the ^{27}Al MAS-NMR spectra analysis, see Table 4.

3.4. ^{23}Na MAS-NMR study

Fig. 5 shows the room temperature ^{23}Na MAS-NMR spectra of $\text{NaTi}_2(\text{PO}_4)_3$ and $\text{NaSn}_2(\text{PO}_4)_3$, given as references. The spectrum of $\text{NaTi}_2(\text{PO}_4)_3$ ($R\bar{3}c$, bottom of Fig. 5) is formed by two sharp peaks at -17.5 and -38.8 ppm and a shoulder (marked with a solid circle) at -53 ppm that corresponds to a unique signal produced. This experimental profile is produced by second-order quadrupole effects, related to the interaction of Na with the electric field gradient at sites with axial symmetry (M1 site). The spectrum of $\text{NaSn}_2(\text{PO}_4)_3$ ($R\bar{3}$, top of Fig. 5) is formed by four sharp peaks at -17.5 , -22 , -34 and -39 ppm and two shoulders at -46 and -52 ppm that correspond to the two expected signals produced by the two non-equivalent M1 sites in the $R\bar{3}$ s.g. [29].

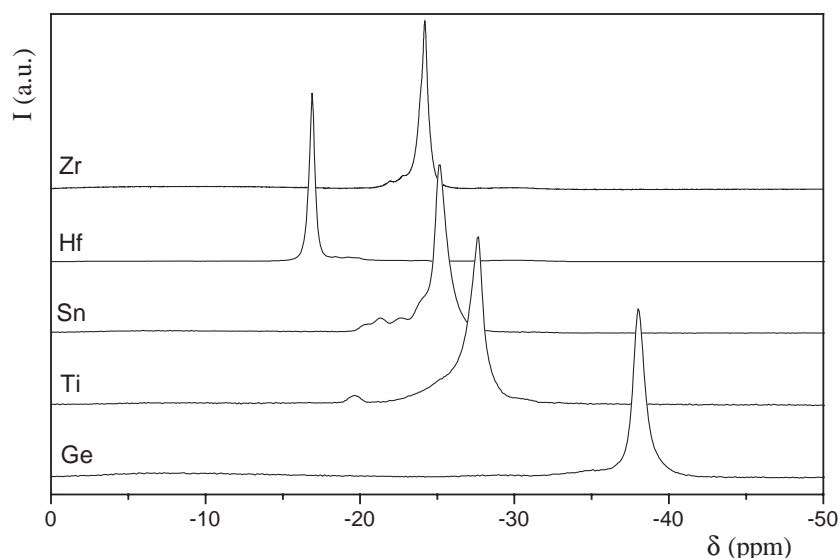


Fig. 4. Centerbands of ^{31}P MAS-NMR spectra for nominal $\text{Na}_{1.4}\text{Al}_{0.4}\text{M}_{1.6}(\text{PO}_4)_3$ (M=Ge, Sn, Ti, Hf and Zr) samples.

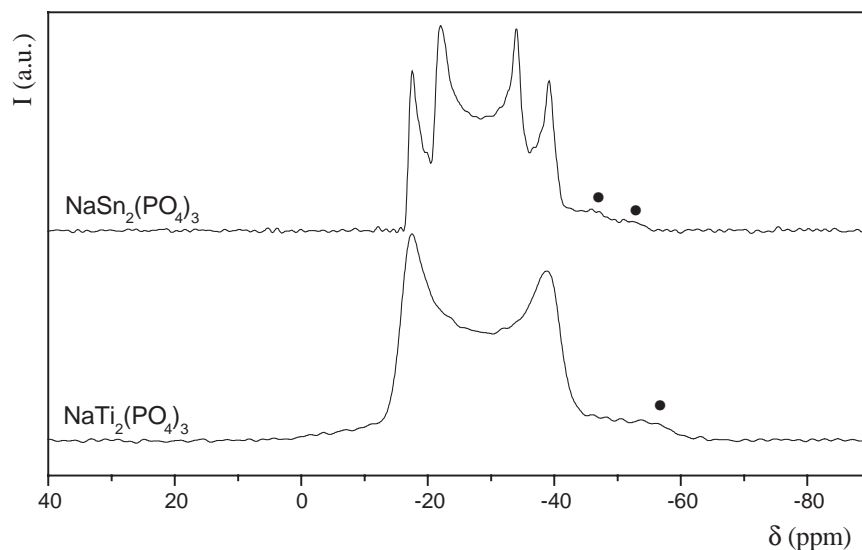


Fig. 5. Centerbands of ^{23}Na MAS-NMR spectra for $\text{NaTi}_2(\text{PO}_4)_3$ and $\text{NaSn}_2(\text{PO}_4)_3$. Shoulders are marked with solid circles.

Fig. 6 shows the room temperature ^{23}Na MAS-NMR spectra for the nominal $\text{Na}_{1.4}\text{Al}_{0.4}\text{M}_{1.6}(\text{PO}_4)_3$ ($\text{M}=\text{Ge}, \text{Sn}, \text{Ti}, \text{Hf}, \text{Zr}$) series. The ^{23}Na spectra for $\text{M}=\text{Ti}, \text{Hf}, \text{Zr}$ samples correspond to sodium atoms localized at a unique M1 site ($R\bar{3}c$). On the other hand, the spectra for $\text{M}=\text{Ge}, \text{Sn}$ samples correspond to sodium atoms situated at two different M1 sites of the NASICON structure with $R\bar{3}$ symmetry. The derived isotropic chemical shifts (σ_{iso}) and quadrupole constants (C_Q) for the five samples are given in Table 6. In the ^{23}Na MAS-NMR spectra of $\text{M}=\text{Ge}, \text{Sn}, \text{Hf}$ and Zr samples, there is not a clear signal corresponding to Na(2) cations. However, in the ^{23}Na spectrum for $\text{M}=\text{Ti}$ contains a shoulder at ~ -9 ppm (marked with a triangle in

Fig. 6) which has been ascribed to Na(2) cations in agreement with previous reports [17].

3.5. Impedance study

The electrical characterization has only been carried out for the materials with the highest aluminum content ($\text{M}=\text{Ge}, \text{Sn}$ and Ti), and so, with the highest sodium carrier concentrations. Some results from the impedance study of $\text{M}=\text{Ti}$ are shown in Figs. 7 and 8. These data are typical for the three compositions. The complex impedance plane plot for $\text{M}=\text{Ti}$, Fig. 7, shows a very broad arc at room temperature where, at least, two well-resolved components

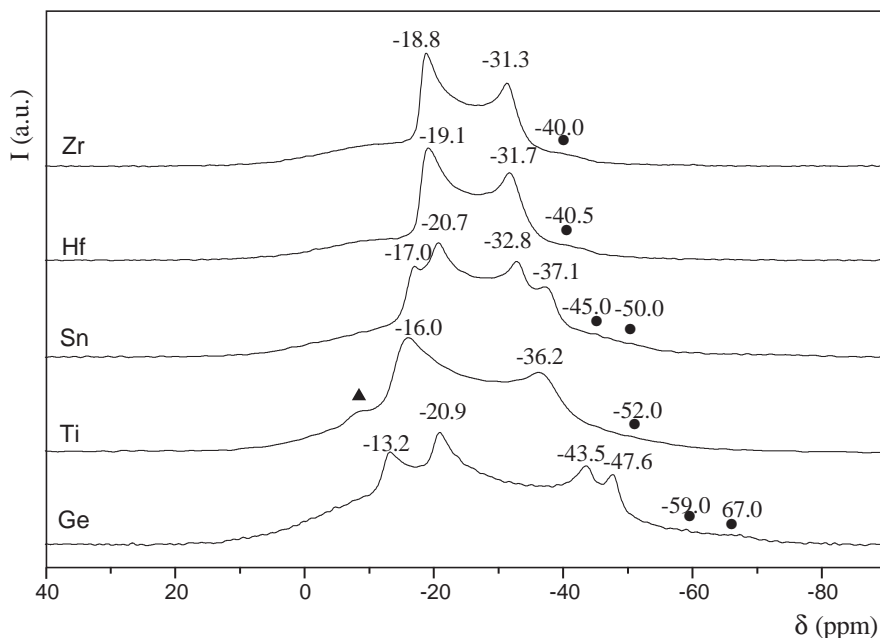


Fig. 6. Centerbands of ^{23}Na MAS-NMR spectra for nominal $\text{Na}_{1.4}\text{Al}_{0.4}\text{M}_{1.6}(\text{PO}_4)_3$ ($\text{M}=\text{Ge}, \text{Sn}, \text{Ti}, \text{Hf}, \text{Zr}$) samples. Up-field shoulders are marked with solid circles and the small signal of Na(2) is marked with a triangle in the Ti sample.

Table 6

Isotropic chemical shift, σ_{iso} , of M1 site and quadrupole constants, C_Q , in ^{23}Na MAS-NMR spectra for $\text{Na}_{1.4}\text{Al}_{0.4}\text{M}_{1.6}(\text{PO}_4)_3$ (M=Ge, Sn, Ti, Hf and Zr) samples

	$\sigma_{\text{iso}}/\text{ppm}$	C_Q/MHz
Ge	−12.9	1490.7
	−2.3	1810.0
Sn	−16.4	1101.6
	−9.8	1425.9
Ti	−8.3	1461.4
Hf	−14.3	1145.0
Zr	−14.6	1120.0

can be distinguished. These components are due to the presence of several contributions to the electrical response of the pellets. At higher temperatures, 473 K (see inset), a well-developed spike can be observed with an associated capacitance of $\sim 0.3 \mu\text{F}$ (20 Hz). Since it is inclined to the Z' axis at $\approx 60^\circ$, it indicates a blocking electrode response, therefore, the conducting species must be ionic, likely, Na^+ ions.

A deeper insight into the electrical microstructure of the pellets can be obtained from the spectroscopic plots of the impedance imaginary part, Z'' , and the complex electric modulus, M'' , vs. $\log f$, see inset in Fig. 8. The Z'' plots show a broad peak with a smooth shoulder at lower frequencies (marked with an asterisk) and the M'' plot a broad peak with an associated capacitance at the maximum very close to that of the Z'' peak. The maxima of both curves are only separated by 0.4 decades in frequency. Hence, these maxima are due to the bulk/intrinsic response of the sample. The shoulder in the overall Z'' plot, with an associated capacitance of 11.4 pF, is very likely due to a grain boundary contribution. Because of the high capacitance of this contribution, it is not readily seen in the M'' spectrum, but it is important in the overall pellet impedance response.

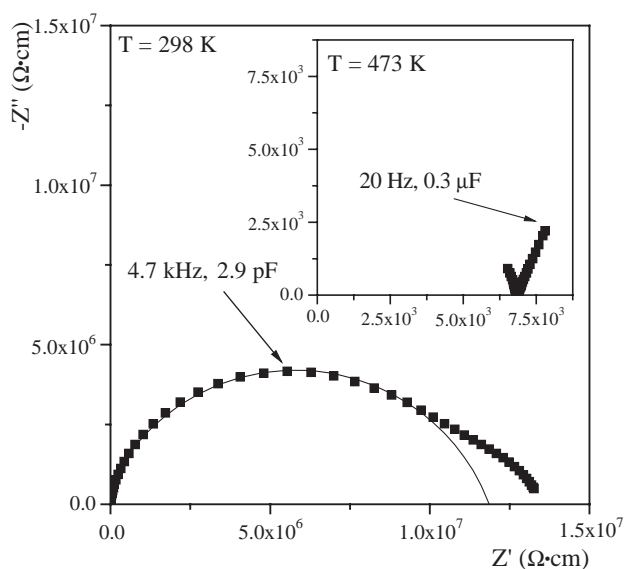


Fig. 7. Complex impedance plane plot for nominal $\text{Na}_{1.4}\text{Al}_{0.4}\text{Ti}_{1.6}(\text{PO}_4)_3$ at 298 K (473 K in the inset).

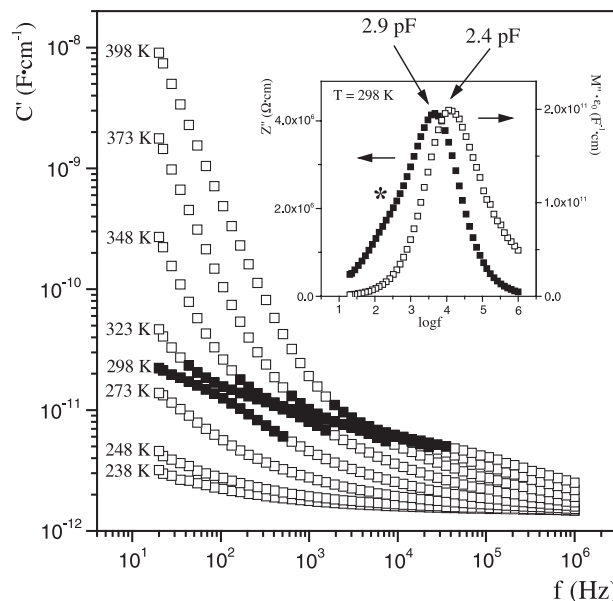


Fig. 8. Real part of the complex capacitance vs. frequency at several selected temperatures for nominal $\text{Na}_{1.4}\text{Al}_{0.4}\text{Ti}_{1.6}(\text{PO}_4)_3$. Highlighted points stand for the thick grain boundary relaxation. The inset shows the spectroscopic plots of Z'' and M'' vs. $\log f$ at 298 K.

To further examine this point, we have plotted the real part of the complex capacitance as a function of frequency for this sample, see Fig. 8. At low frequency and high temperature a blocking electrode effect can be observed. At higher frequencies and lower temperatures, the curves show a clear relaxation from $\sim 10 \text{ pF}$ to lower values in the pF range as frequency increases (black highlighted points). This relaxation is attributed to a thick grain boundary at the region of grain–grain contacts. This can not be observed in

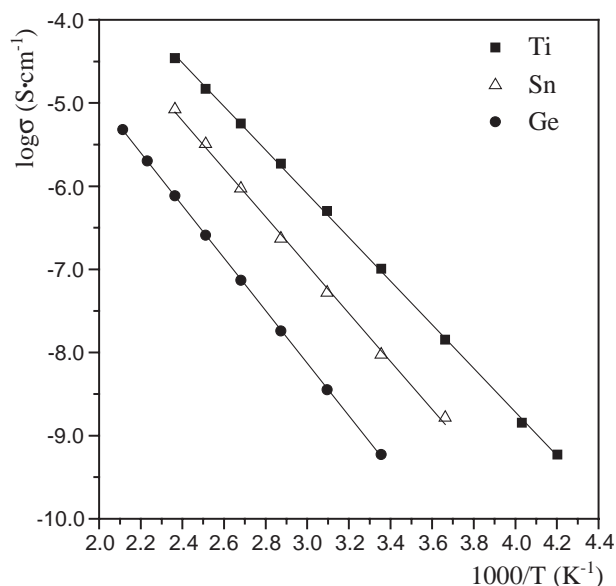


Fig. 9. Variation of $\log \sigma_T$ versus $1000/T$ for nominal $\text{Na}_{1.4}\text{Al}_{0.4}\text{Ti}_{1.6}(\text{PO}_4)_3$ (■), $\text{Na}_{1.4}\text{Al}_{0.4}\text{Sn}_{1.6}(\text{PO}_4)_3$ (△) and $\text{Na}_{1.4}\text{Al}_{0.4}\text{Ge}_{1.6}(\text{PO}_4)_3$ (●).

Table 7

Overall ionic conductivities at 400 K and activation energies for nominal $\text{Na}_{1.4}\text{Al}_{0.4}\text{M}_{1.6}^{\text{IV}}(\text{PO}_4)_3$ (M=Ge, Sn, Ti) samples

$(\text{Al}/\text{In}^{3+}, \text{M}^{4+})_2$	$\sigma_T(400 \text{ K})/\text{S cm}^{-1}$	E_a/eV	$E_a^{\#}/\text{eV}$
$\text{Al}_{0.13}\text{Ge}_{1.87}$	$2.8(3) \cdot 10^{-7}$	0.63(1)	0.62(1)
$\text{Ge}_2^{\&}$	$2.2 \cdot 10^{-11}$	1.02	—
$\text{Al}_{0.15}\text{Sn}_{1.85}$	$3(1) \cdot 10^{-6}$	0.57(1)	0.56(1)
$\text{In}_{0.4}\text{Sn}_{1.6}^*$	$3.9 \cdot 10^{-6}$	0.53	0.58
$\text{Sn}_2^{\&}$	$4.5 \cdot 10^{-9}$	0.58	—
$\text{Al}_{0.30}\text{Ti}_{1.70}$	$1.5(3) \cdot 10^{-5}$	0.52(1)	0.53(1)
$\text{In}_{0.4}\text{Ti}_{1.6}^*$	$2.8 \cdot 10^{-6}$	0.54	0.60
$\text{Ti}_2^{\&}$	$3.7 \cdot 10^{-7}$	0.47	—

Electrical data for parent $\text{Na}_{1.6}\text{M}_2(\text{PO}_4)_3$ (M=Ge, Sn, Ti) compounds and $\text{Na}_{1.4}\text{In}_{0.4}\text{M}_{1.6}^{\text{IV}}(\text{PO}_4)_3$ (M=Ti, Sn) analogous samples are also included for the sake of comparison. E_a obtained from Arrhenius plot of $\log f_{\max} [M'']$.

$\&$ Data taken from [10]. $*$ Data taken from [16].

modulus plots because the modulus scales with the inverse of the capacitance.

Total pellet conductivities, σ_T , were obtained from the intercept of the spike and/or the arc (low frequency end) on the Z' axis in Nyquist plots. Fig. 9 shows the overall conductivity data plotted as $\log \sigma_T$ vs. $1000/T$ for $\text{Na}_{1.4}\text{Al}_{0.4}\text{M}_{1.6}(\text{PO}_4)_3$ (M=Ge, Sn and Ti). Conductivity data at 400 K and activation energies (E_a) obtained from these representations are listed in Table 7. Activation energies obtained from the non-conventional Arrhenius plot of the frequency of the modulus peak maxima (not shown) are also listed in Table 7. Electrical data for the parent phases and those for In-doped analogous compounds are also given for the sake of comparison.

4. Discussion

Aluminum contents in the nominal NASICON $\text{Na}_{1.4}\text{Al}_{0.4}\text{M}_{1.6}(\text{PO}_4)_3$ (M=Ge, Sn, Ti, Zr, Hf) compounds, derived from three independent techniques are given in Table 8. It can be seen that aluminum contents deduced from the ^{31}P and ^{23}Na MAS-NMR spectra and the joint Rietveld refinements of the NPD and LXRPD data are in good agreement but they are smaller than the expected ones. However, the amount of aluminum in the side crystalline phases (AlPO_4 and NaAlP_2O_7) is lower than that not incorporated in the NASICON phases. In order to understand this fact, we added a weighted crystalline standard, MgO 20.01 wt.%, to the M=Ge sample prior to the NPD data collection. From the overestimation of the refined phase fraction, 2.7(1) wt.%, the non-diffracting (amorphous) content of this sample was 14.8(6) wt.%. Hence, the phase composition of the nominal $\text{Na}_{1.4}\text{Al}_{0.4}\text{Ge}_{1.6}(\text{PO}_4)_3$ sample is $\text{Na}_{1.13}\text{Al}_{0.13}\text{Ge}_{1.87}(\text{PO}_4)_3$ 80.2 wt.%, AlPO_4 4.4 wt.%, GeO_2 0.6 wt.% and amorphous 14.8 wt.%. So, the excess of sodium and aluminum, not incorporated in the crystalline phases, must form part of the amorphous phase.

The aluminum content is maximum along the studied family for the M=Ti sample, as shown in Table 8. This may

be justified because the ionic radius of Ti^{4+} is the closest to that of Al^{3+} in the samples with the metals of d-block (M=Ti, Zr and Hf) which have $R\bar{3}c$ symmetry. On the other hand, the samples with metals of p-block (M=Ge and Sn) have $R\bar{3}$ symmetry which display lower Al^{3+} aliovalent substitutions.

This conclusion is supported by the analysis of the ^{27}Al NMR spectra, Fig. 3. In addition to the main NASICON peak, there are broad bands in the AlO_6 region, close to -15 ppm, which cannot be justified as arising from the NASICON phases. Furthermore, the large integrated area of the 39 ppm broad band, AlO_4 groups, can not only be due to small amounts of detected AlPO_4 , see Table 1. For instance, nominal $\text{Na}_{1.4}\text{Al}_{0.4}\text{Hf}_{1.6}(\text{PO}_4)_3$ sample contains only 3.2 wt.% of AlPO_4 but the peak at 40 ppm is very large. Hence, the amorphous phase(s) must contain aluminum in both octahedral and tetrahedral environments.

As it was shown in the results section, the Na(1) signal in the ^{23}Na MAS-NMR spectra is formed by a set of three bands in the $R\bar{3}c$ s.g. and two sets of three bands in the $R\bar{3}$ s.g., see Fig. 6. In all cases, experimental profiles correspond to Na ions located in crystallographic Na1 sites displaying axial symmetry ($\eta=0$). The separation between the maxima for the Na(1) NASICON signals increases as the tetravalent cation radii and more specifically as the Na–O distances decrease. In particular, it can be observed that C_Q values are 1800, 1450 and 1100 kHz when M–O distances are near to 2.40 (Ge1b sites), 2.47 (Ge1a, Sn1b and Ti sites) and 2.55 Å (Sn1a and Hf sites). This is due to the progressive distortion produced in octahedra, which increases electrical field gradients at occupied sites, when M–O distances and cell edge parameters decrease [29]. The structural study showed that Na cations preferentially occupy Na1 sites and extra sodium incorporated in M2 sites is low except for the titanium sample. This is in agreement with the ^{23}Na NMR study, see Fig. 6, where the Na(2) signal was only evident in the M=Ti sample as a shoulder at -9 ppm [17]. Finally, the presence of sodium into the amorphous phase is readily evident in these spectra as a broad band in ^{23}Na NMR spectra which is spread over a very large chemical shift range.

It is difficult to analyze the evolution of the a , c and V unit cell parameters along the nominal $\text{Na}_{1.4}\text{Al}_{0.4}\text{M}_{1.6}(\text{PO}_4)_3$ (M=Ge, Ti, Sn, Hf, Zr) series because the aluminum contents of the samples are different. As a general trend,

Table 8

Aluminum molar contents in the octahedral site(s) deduced from ^{31}P and ^{27}Al MAS-NMR spectra and joint LXRPD and NPD Rietveld refinements for nominal $\text{Na}_{1.4}\text{Al}_{0.4}\text{M}_{1.6}^{\text{IV}}(\text{PO}_4)_3$ (M=Ge, Sn, Ti, Hf and Zr) samples

	Al_x (^{31}P NMR)	Al_x (^{27}Al NMR)	Al_x (Rietveld)
Ge	0.08	0.12	0.13
Sn	0.15	0.19	0.15
Ti	0.21	0.31	0.30
Hf	0.05	0.04	0.09
Zr	0.05	0.06	—

these parameters (see Table 1) increases in the sequence $\text{Ge} < \text{Ti} < \text{Sn} < \text{Hf} < \text{Zr}$, which is in agreement with the variation in the ionic radii of the tetravalent cations [30]. Hence, it seems more appropriated to compare the unit cell parameters of $\text{Na}_{1+x}\text{Al}_x\text{M}_{2-x}(\text{PO}_4)_3$ ($\text{M} = \text{Ge}, \text{Sn}, \text{Ti}, \text{Hf}, \text{Zr}$) compounds with those of the $\text{NaM}_2(\text{PO}_4)_3$ ($\text{M} = \text{Ge}, \text{Sn}, \text{Ti}, \text{Hf}, \text{Zr}$) pristine materials given in Table 1. The unit cell changes are small and it depends upon the symmetry of the starting material. As the aluminum (and the corresponding sodium to counterbalance the charges) is introduced into the NASICON phase, the unit cell volume increases for $\text{M} = \text{Ge}$ and Sn ($R\bar{3}$ s.g.) and decreases for $\text{M} = \text{Ti}, \text{Zr}$ and Hf ($R\bar{3}c$ s.g.), see Table 1. The aliovalent substitution of $\text{M}(\text{IV})$ by smaller $\text{Al}(\text{III})$ yields the expected $\text{M}-\text{O}$ average bond distance contraction, see Table 1. However, the anisotropic nature of the NASICON structure plus the introduction of the extra sodium do not allow to directly reflect this contraction in the a and c unit cell parameters.

In view of the low incorporation of aluminum into the $\text{M} = \text{Zr}$ and Hf phases, electrical characterization has only been carried out for $\text{M} = \text{Ge}, \text{Sn}$ and Ti samples. $\text{M} = \text{Ti}$ composition exhibits higher Na^+ conductivity and lower activation energy than $\text{M} = \text{Ge}$, and Sn samples, see Fig. 9 and Table 7. However, a direct comparison of the conductivity of these phases cannot be carried out as the aluminum contents in the NASICON phases are not the same. It must be noted that $\text{M} = \text{Ti}$ samples have the highest aluminum content, $\text{Na}_{1.30}\text{Al}_{0.30}\text{Ti}_{1.70}(\text{PO}_4)_3$.

Long-range conduction of the ions in the NASICON structure involves hopping between the M1 and M2 sites. As explained in the introduction section, these sites are connected by bottlenecks, generally termed the M1M2 and M2M2 bottlenecks. Taking into account the Na radius, the direct hopping between two M2 sites is not possible because of the small M2M2 bottleneck size. Hence, only M1–M2–M1 conduction pathways are relevant in these materials. We have used bond valence calculations to predict the conduction geometry on the basis of the oxygen sublattice for $\text{Na}_{1.15}\text{Al}_{0.15}\text{Sn}_{1.85}(\text{PO}_4)_3$, $\text{Na}_{1+x}\text{Al}_x\text{Ti}_{2-x}(\text{PO}_4)_3$ ($x = 0.4$ and 0.8) and $\text{Na}_{1+x}\text{In}_x\text{Zr}_{2-x}(\text{PO}_4)_3$ ($x = 0.8$ and 1.6). For these type of studies, the oxygen sublattice must be known accurately and so, structural data derived from Rietveld refinements including NPD data must be used (i.e. LXRPD data analyses are not suitable). Structural data for $\text{Na}_{1+x}\text{In}_x\text{Zr}_{2-x}(\text{PO}_4)_3$ ($x = 0.8$ and 1.6) were obtained from [17].

As previously described [31,32], bond valence sum $\Phi(x,y,z)$ is calculated for any arbitrary point (x,y,z) of the conduction pathway of the NASICONs taking into account the oxygen sublattice. By moving the arbitrary point (x,y,z) over a grid covering the whole unit cell volume, one can find the probable trajectory for the Na^+ ions. This can be done by following the points with lowest $\Phi(x,y,z)$ starting from a specified position (e.g., Na1) and following a certain initial direction (e.g. toward Na2). Then, this direction is not fixed during the path, and the ion is left free to direct itself following the lowest $\Phi(x,y,z)$ way inside a solid angle

within an iterative process. We have carried out all calculations using the JUMPIER program [31]. The valence sum for Na^+ ion can be plotted versus the distance traveled along, thus, obtaining a plot of $\Phi(d)$ versus d (Å). Saddle points of the $\Phi(d)$ function correspond to potential barrier (bottlenecks) encountered by the ion along its trajectory.

Fig. 10(a) shows the $\Phi(d)$ curve for $\cdots\text{Na1}-\text{Na2}\cdots$ conduction paths in $\text{Na}_{1.15}\text{Al}_{0.15}\text{Sn}_{1.85}(\text{PO}_4)_3$ which crystallizes in $R\bar{3}$. Fig. 10(b) and (c) show similar $\Phi(d)$ curves for $\text{Na}_{1+x}\text{Al}_x\text{Ti}_{2-x}(\text{PO}_4)_3$ ($x = 0.4$ and 0.8) and $\text{Na}_{1+x}\text{In}_x\text{Zr}_{2-x}(\text{PO}_4)_3$ ($x = 0.8$ and 1.6) samples, respectively, which crystallize in $R\bar{3}c$. It can be noticed that for $\text{M} = \text{Sn}$ composition (see Fig. 10(a)), there are three crystallographic sites for Na^+ : two non-equivalent M1 (M1a and M1b) and one M2. These three sodium positions, surrounded by their corresponding oxygens, yield three different valence sum minima. The oxygen environment around M1b is more suitable for sodium cations (lower valence sum) than that around M1a. Furthermore, the $\Phi(d)$ curve identifies the two potential barriers (bottlenecks), M1aM2 and M1bM2, with slightly different valence sums and shapes. The curve $\Phi(d)$ for $\text{Na}_{1.13}\text{Al}_{0.13}\text{Ge}_{1.87}(\text{PO}_4)_3$ is very similar to that of $\text{M} = \text{Sn}$.

On the other hand, $\text{M} = \text{Ti}$ and Zr samples show one M1 and one M2 sites ($R\bar{3}c$ s.g.), with a unique potential barrier, M1M2 bottleneck, see Fig. 10(b) and (c). Fig. 10(b) shows that the valence sum bottleneck maximum for $\text{TiAl}_{0.8}$ is higher than that for $\text{TiAl}_{0.4}$, in agreement with the E_a values, 0.55 eV for $\text{TiAl}_{0.8}$ and 0.53 eV for $\text{TiAl}_{0.4}$ [18]. This behavior is also observed for the ZrIn_x samples, where the valence sum at the bottleneck for $\text{ZrIn}_{1.6}$ is higher than that for $\text{ZrIn}_{0.8}$, and E_a value for $\text{ZrIn}_{1.6}$ (0.46 eV) is larger than that of $\text{ZrIn}_{0.8}$ (0.42 eV) [17]. When comparing both series, it can be seen that $\Phi(d)$ curves for ZrIn_x samples are much lower than those for TiAl_x and nearer to 1.0 (ideal value for Na^+ ion). Again, this fact is in accordance with the lower activation energies and higher conductivity values measured for the ZrIn_x series. Thus, we can conclude that the sodium conduction pathway size is more appropriate in the $\text{Na}_{1+x}\text{In}_x\text{Zr}_{2-x}(\text{PO}_4)_3$ series than in the analogous $\text{Na}_{1+x}\text{Al}_x\text{Ti}_{2-x}(\text{PO}_4)_3$ series.

Finally, its worth to note that the activation energy for $\text{Na}_{1.15}\text{Al}_{0.15}\text{Sn}_{1.85}(\text{PO}_4)_3$ (0.56 eV) is higher than those of the TiAl_x and ZrIn_x series in agreement with the $\Phi(d)$ curves where the bottlenecks have slightly higher valence sums. Furthermore, the valence differences between the maximum and the minimum of the $\Phi(d)$ curves are 0.48 (between M1b and M1bM2 bottleneck), 0.36 and 0.26 valence units for $\text{M} = \text{Sn}, \text{Ti}, \text{Zr}$ samples, respectively. This trend is in close agreement with the differences in the measured activation energies for the sodium ion conduction process.

All these considerations have been deduced on the basis that Na1 and Na2 sites are not simultaneously occupied. However, in the samples analyzed Na1–Na2 electrostatic repulsions must favor dispersion of Na cations in conduction networks. Hence, full occupancy of Na1 sites can

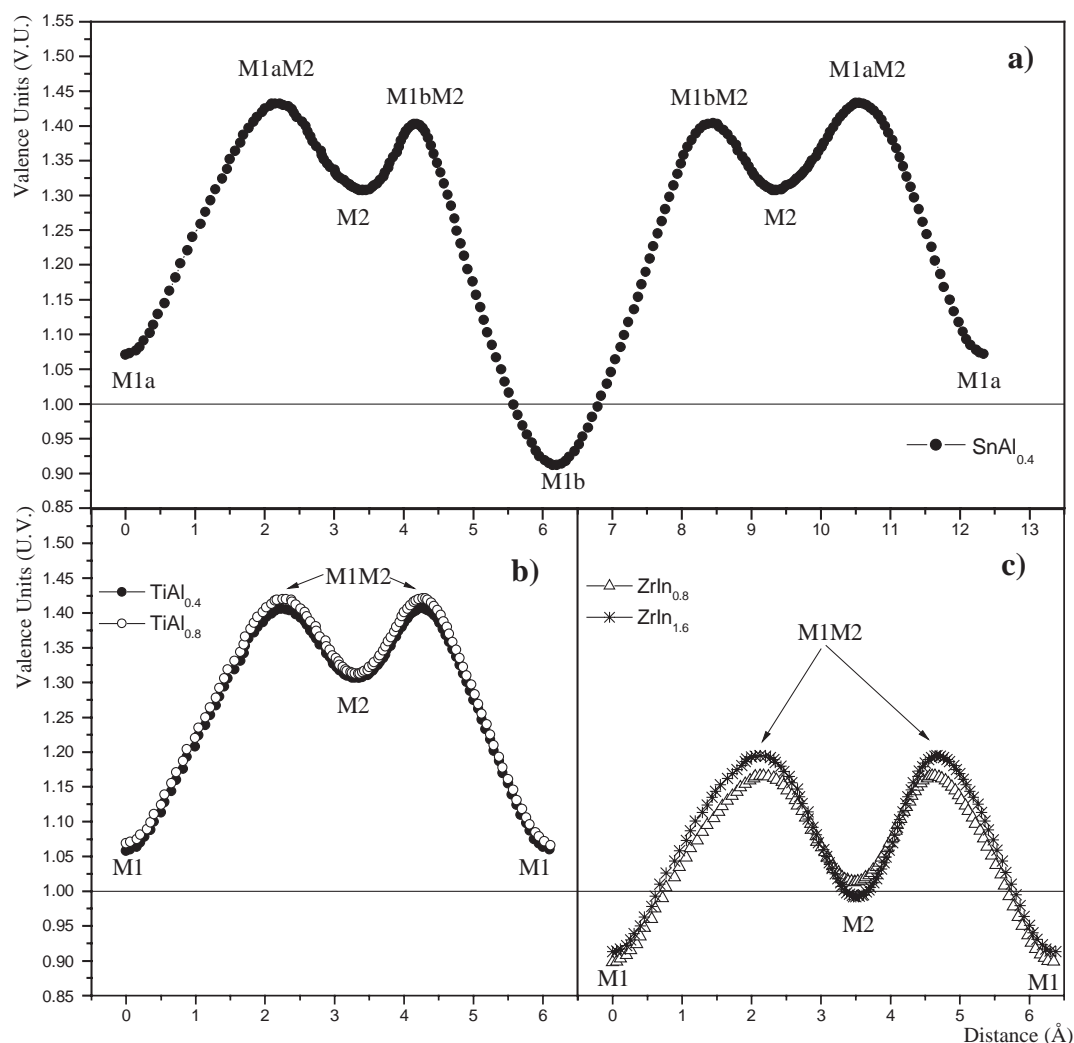


Fig. 10. $\Phi(d)$ curves for $\cdots\text{Na1}-\text{Na2}\cdots$ conduction paths in (a) $\text{Na}_{1.4}\text{Al}_{0.4}\text{Sn}_{1.6}(\text{PO}_4)_3$; (b) $\text{Na}_{1+x}\text{Al}_x\text{Ti}_{2-x}(\text{PO}_4)_3$ ($x=0.4$ and 0.8) and (c) $\text{Na}_{1+x}\text{In}_x\text{Zr}_{2-x}(\text{PO}_4)_3$ ($x=0.8$ and 1.6).

not likely be produced. Taken into account that symmetry-related infinite channels running in different directions are interconnected at M1 sites, a slight decrease of Na1 occupation must improve configurational entropy (cation disorder) in the analyzed compounds. This may explain that activation energy does not increase with respect to the pristine materials, but ion conductivity increases 2–3 orders of magnitude. Similar results were reported for $\text{Na}_{1+x}\text{In}_x\text{Zr}_{2-x}(\text{PO}_4)_3$ series [17]. For $\text{M}=\text{Ge}$, where unit cell parameters increase in a significant way, activation energy decreases considerably, probably as a consequence of geometrical changes produced in bottlenecks connecting M1 and M2 sites.

5. Conclusions

$\text{Na}_{1.4}\text{Al}_{0.4}\text{M}_{1.6}(\text{PO}_4)_3$ ($\text{M}=\text{Ge}, \text{Sn}, \text{Ti}, \text{Hf}, \text{Zr}$) compositions have been prepared, however, the incorporated

aluminum contents into the main NASICON phases are always smaller than the nominal contents used in the preparations. The non-incorporated Al is present in the crystalline side-phases (f.i. AlPO_4) and in an amorphous fraction (likely sodium aluminate and sodium aluminum phosphate). The main NASICON phase have $R\bar{3}$ symmetry for $\text{M}=\text{Ge}$ and Sn and $R\bar{3}c$ symmetry for $\text{M}=\text{Ti}, \text{Hf}, \text{Zr}$. Joint NPD and LXRPD data analysis by the Rietveld method has allowed to obtain an accurate description of the structures of these materials. ^{27}Al , ^{31}P and ^{23}Na MAS-NMR spectroscopies also shed light over the stoichiometries and local environments of atoms in these samples. The optimum aluminum doping is produced in the $\text{M}=\text{Ti}$ phase, which displays the lowest activation energy and the maximum conductivity. The analysis of the bond valence sum along different possible trajectories, has shown that the most probable conduction pathway for Na cations is $\text{Na1}-\text{Na2}-\text{Na1}$ in the analyzed compositions.

Acknowledgements

We thank Prof. Mazza (Politecnico di Torino, Italy) for providing the JUMPIER program and for the fruitful discussions. This work was partially performed at the spallation neutron source SINQ, Paul Scherrer Institut, Villigen, Switzerland, and we also thank Dr. D.V. Sheptyakov for his assistance during the SINQ experiment. The financial support from MAT2003-7483-C2-1 research grant is acknowledged.

A. Supplementary data

Supplementary data associated with this article can be found, in the online version, at [doi:10.1016/j.ssi.2005.04.009](https://doi.org/10.1016/j.ssi.2005.04.009).

References

- [1] H.Y.-P. Hong, *Mater. Res. Bull.* 11 (1976) 173.
- [2] J.B. Goodenough, H.Y.-P. Hong, J.A. Kafalas, *Mater. Res. Bull.* 11 (1976) 203.
- [3] H. Kohler, H. Schulz, *Solid State Ionics* 9–10 (1983) 795.
- [4] H. Kohler, H. Schulz, *Mater. Res. Bull.* 20 (1985) 1461.
- [5] H. Kohler, H. Schulz, *Mater. Res. Bull.* 21 (1986) 23.
- [6] J.L. Rodrigo, J. Alamo, *Mater. Res. Bull.* 26 (1991) 475.
- [7] J. Alamo, J.L. Rodrigo, *Mater. Res. Bull.* 27 (1992) 1091.
- [8] H. Aono, E. Sugimoto, *J. Am. Ceram. Soc.* 79 (10) (1999) 2786.
- [9] C. Verissimo, F.M.S. Garrido, O.L. Alves, P. Calle, A. Martinez-Juarez, J.E. Iglesias, J.M. Rojo, *Solid State Ionics* 100 (1997) 127.
- [10] J.M. Winand, A. Rulmont, P.J. Tarte, *Solid State Ionics* 93 (1991) 341.
- [11] M.P. Carrasco, M.C. Guillem, J. Alamo, *Mater. Res. Bull.* 27 (1992) 603;
M.P. Carrasco, M.C. Guillem, J. Alamo, *Mater. Res. Bull.* 28 (1993) 547;
M.P. Carrasco, M.C. Guillem, J. Alamo, *Mater. Res. Bull.* 28 (1993) 793.
- [12] M.P. Carrasco, M.C. Guillem, J. Alamo, *Solid State Ionics* 63–65 (1993) 684;
M.P. Carrasco, M.C. Guillem, J. Alamo, *Solid State Ionics* 63–65 (1993) 688.
- [13] M.P. Carrasco, M.C. Guillem, J. Alamo, *Mater. Res. Bull.* 29 (1994) 817.
- [14] Y. Miyajima, T. Miyoshi, J. Tamaki, M. Matsuoka, Y. Yamamoto, C. Masquelier, M. Tabuchi, Y. Saito, H. Kageyama, *Solid State Ionics* 124 (1999) 201.
- [15] S. Patoux, G. Rousse, J.B. Leriche, C. Masquelier, *Chem. Mater.* 15 (2003) 2084.
- [16] E.R. Losilla, M.A.G. Aranda, S. Bruque, M.A. Paris, J. Sanz, A.R. West, *Chem. Mater.* 10 (1998) 665.
- [17] E.R. Losilla, M.A.G. Aranda, S. Bruque, J. Sanz, M.A. Paris, J. Campo, A.R. West, *Chem. Mater.* 12 (2000) 2134.
- [18] F.E. Mouahid, M. Bettach, M. Zahir, P. Maldonado-Manso, S. Bruque, E.R. Losilla, M.A.G. Aranda, *J. Mater. Chem.* 10 (2000) 2748.
- [19] P. Fischer, G. Frey, M. Koch, M. Konnecke, V. Pomjakushin, J. Schefer, R. Thut, N. Schlumpf, R. Burge, U. Greuter, S. Bondt, E. Beruier, *Physica B* 276–278 (2000) 146.
- [20] H.M.J. Rietveld, *Appl. Crystallogr.* 2 (1969) 65.
- [21] A.C. Larson, R.B. von Dreele, GSAS program, Los Alamos National Lab. Rep. No. LA-UR-86-748 (1994).
- [22] A.G. de la Torre, M.A.G. Aranda, *J. Appl. Crystallogr.* 34 (2001) 196.
- [23] Bruker WINFIT program, Bruker-Rep. 140 (1994) 43.
- [24] Novocontrol GmbH, WinDETA Owner's Manual, Hundsangen, Germany, 1995.
- [25] R. Shimanouchi-Futagami, H. Nishizawa, *Kin. Daigaku Rik. Kenk. Hokoku* 16 (1995) 13.
- [26] L.O. Hagman, P. Kierkegaard, *Acta Chem. Scand.* 22 (1968) 1822.
- [27] P. Thompson, D.E. Cox, J.B. Hastings, *J. Appl. Crystallogr.* 20 (1987) 79.
- [28] L.W. Finger, D.E. Cox, A.P. Jephcoat, *J. Appl. Crystallogr.* 27 (1994) 892.
- [29] N.J. Clayden, L.J. Pugh, *Mater. Sci. Lett.* 17 (1998) 1563.
- [30] R.D. Shannon, *Acta Crystallogr., A* 32 (1976) 751.
- [31] D. Mazza, *J. Solid State Chem.* 156 (2001) 154.
- [32] P. Maldonado-Manso, E.R. Losilla, M. Martinez-Lara, M.A.G. Aranda, S. Bruque, F.E. Mouahid, M. Zahir, *Chem. Mater.* 15 (2003) 1879.